High strain rate tensile behavior of a quenching and partitioning (Q&P) Fe-0.25C-1.5Si-3.0Mn steel

Peikang. Xia [a, b, *], F. Vercruysse [c], Roumen Petrov [c d],

Ilchat Sabirov [a], Miguel Castillo-Rodríguez [a], Patricia Verleysen [c]

[a] IMDEA Materials Institute, Calle Eric Kandel 2, Getafe, 28906 Madrid, Spain

[b] Universidad Politécnica de Madrid, E.T.S. de Ingenieros de Caminos, 28040 Madrid, Spain

[c] Department of Electrical Energy, Metals, Mechanical constructions & Systems, Research group Materials Science and Technology, Ghent University, Technologiepark 903, 9052 Gent, Belgium

[d] Delft University of Technology, Department of Materials Science and Engineering, Mekelweg 2, 2628, CD Delft, The Netherlands

Abstract

The mechanical behavior and microstructural evolution of a quenched and partitioned (Q&P) Fe-0.25C-1.5Si-3.0Mn (wt. %) steel were investigated in a wide range of strain rates (10^{-4}–10^{3} s^{-1}). The static tensile tests (10^{-4} and 10^{-2} s^{-1}) were conducted using a universal testing machine, while high strain rate tests (500–1000 s^{-1}) were carried out on a split Hopkinson tensile bar system. High speed camera imaging combined with the digital image correlation (DIC) technique were employed to study homogeneity of plastic deformation. Electron backscatter diffraction (EBSD) and scanning electron microscopy were used to characterize the microstructure evolution in the deformed zone and the fracture surface, respectively. The results indicate that the yield strength of the Q&P steel in dynamic tests (500–1000 s^{-1}) is by 200 MPa higher compared to static tests (10^{-4} and 10^{-2} s^{-1}), while the ultimate tensile strength tends to increase

* Corresponding author.
Peikang Xia, IMDEA Materials Institute, Calle Eric Kandel 2, Getafe, 28906, Madrid, Spain.
Phone: +34 91 549 34 22
E-mail addresses: xia.peikang@imdea.org, xia.peikang@gmail.com

linearly with strain rate. The results of DIC analysis demonstrate that the homogeneity of plastic deformation is similar in static and dynamic test conditions. EBSD characterization shows that the retained austenite (RA) fraction decreases exponentially with the increase of plastic strain during both static and dynamic tensile testing. Additionally, examination of the fracture surfaces reveals the largest dimples in the statically tested specimens.

Keywords: Advanced high strength steel; Quenching and partitioning, High strain rate; Split Hopkinson tensile bar; Digital image correlation

1. Introduction

Light body weight, superior oil efficiency and high passenger security are always the objectives pursued by automobile manufacturers. In the past decades, one of the achievements in seeking more suitable materials for vehicles is the development of advanced high strength steels (AHSSs), that combine high strength and ductility. Significant research activities have been carried out on several types of AHSSs, including transformation induced plasticity (TRIP) steels [1,2], twining induced plasticity (TWIP) steels [3,4], dual phase (DP) steels [5,6] and quenched and partitioned (Q&P) steels [7,8]. As one of the most promising candidates in mass industry application, Q&P steels possess much higher strength compared with TRIP steels and DP steels, and lower alloying elements addition with respect to TWIP steels.

Since the first report by Speer et al. in 2003 [9], Q&P steels have drawn significant attention because of their high strength and improved ductility (with respect to the first generation AHSSs), which is one of the requirements in the automotive sector. The Q&P process contains two steps: (1) a quenching step, which refers to a quenching to the temperature between martensite start temperature (M_s) and martensite finish temperature (M_f) from austenitization temperature or intercritical temperature range; (2) a partitioning step, which involves a direct isothermal holding at or above the quenching

temperature followed by the final quench to room temperature. Carbon diffusion from supersaturated martensite into austenite during the partitioning process results in stabilization of austenite, though during the final quench part of austenite is transformed into martensite due to insufficient stabilization because of too low local carbon content. The latter is referred to as untempered martensite (UM) (or fresh martensite), whereas the martensite formed in the first quench is referred to as tempered martensite (TM). The Q&P treated steels composed of a martensite matrix (UM and TM) and considerable fraction of RA can demonstrate ultimate tensile strength (UTS) exceeding 2000 MPa and total elongation (TE) up to 20 % [10–13]. The high strength of Q&P steels is favorable for reducing weight of car bodies and increasing passenger safety, while the enhanced ductility is beneficial for metal forming operations and provides enhanced energy absorption in crash accidents. These outstanding features make Q&P steels an ideal candidate for structural and safety parts in automobile bodies, such as B-pillar reinforcing parts, cross members, longitudinal beams, sills, and bumper reinforcement [14].

During crash incidents, car body parts are deformed and damaged by high energy in extremely short time period, challenging the capacity of automobile steels to withstand high speed loading. Thus, it is of great importance to understand the mechanical behavior of AHSSs at high strain rates. There is a significant body of research on high strain rate behavior of various types of AHSSs. Experimental investigation on 600/800/1000 MPa DP steels and a 1200 MPa fully martensitic steel showed that DP steels show positive strain rate sensitivity, while negative strain rate sensitivity was observed for martensitic steels [15]. A significant strain rate sensitivity was reported for a tempered martensitic steel in [16]. The mechanical behavior was modelled as a function of strain rate using a dislocations dynamics model based on net storage of dislocations. The parameters of the model were determined and then used to predict the deformation range of the tensile deformation stability. In the study, however, adiabatic heating effects were not taken into account in the analysis of the high strain rate tests [16]. Indeed, at high strain rates, plastic work converted into heat results in a temperature increase of the sample material. The latter can significantly affect the flow

stress and, if ignored, give rise to erroneous values of the strain rate sensitivity [17]. Study of four low carbon TRIP steels [18] and three different TRIP steels [19] showed that their mechanical properties increase with increasing strain rate. No austenite transformation at strain rates above 1000 s^{-1} was observed on 1 wt. % Al added TWIP steel and on 3.5 wt. % Al added TWIP steel, the restricted strain rate was 720 s^{-1} [20]. Liang et al. verified the suppression of deformation twins at high strain rates via synchrotron X-ray diffraction measurements [21].

Most publications on Q&P steels focused either on microstructure optimization and evolution or on improvement of the strength and ductility [7,8,12,22–26], whereas the high strain rate deformation behavior has not been deeply investigated yet. Therefore, it is of great importance to gain a fundamental understanding on their mechanical behavior and microstructure evolution at high strain rate, though it is a very challenging task due to complex microstructure [27,28]. The goal of the present work is to contribute to a better understanding of the mechanical behavior and the corresponding microstructural changes in static and dynamic conditions of a Fe-0.25C-1.5Si-3.0Mn (wt. %) steel after Q&P treatment.

2. Experimental procedures

2.1. Material and processing

The chemical composition of the studied Q&P steel is shown in Table 1. A medium carbon content (0.25 wt. %) was adopted to achieve sufficient RA volume fraction and stability [29]. 3 wt. % of manganese was chosen to enhance the hardenability and stability of RA [30,31], as segregation of Mn and a band structure would appear if a higher amount of Mn is added [32,33]. The silicon was limited to 1.5 wt. % to suppress carbide formation [34,35] without degradation of galvanisability [36]. Small amounts of aluminum (0.023 wt.%) and chromium (0.015 wt.%) were also added to inhibit cementite formation [37] and improve hardenability [38]. Obviously, the fractions of Al and Cr are too low to delay the cementite or bainite formation, however, together with 1.5% Si, cementite formation is effectively suppressed in steels [34,35].

Table 1 Chemical composition (wt. %) of the steel used in this study.

C	Mn	Si	Al	Cr
0.25	3.0	1.5	0.023	0.015

A laboratory vacuum induction furnace was used for casting the selected steel. After casting, the steel slabs were hot rolled to a final thickness of 2.5 mm, cooled by water jets to 600 °C and transferred to a furnace for coiling simulations at 560 °C. Then the hot rolled plates of the studied steel grades were pickled and cold rolled to a thickness of 1 mm (imposing 60% of cold reduction). The achieved rolled steel strips were cut perpendicular to the rolling direction and then subjected to Q&P heat treatment in a reactive annealing process simulator, as schematically shown in Fig. 1. The samples were heated up to 850 °C for 60s for full austenitization and then quenched to the quenching temperature (QT) of 244 °C at the rate of 20 °C/s. Finally, after reheating to the partitioning temperature (PT) of 400 °C and isothermally holding for 500 s (partitioning time, Pt), samples were quenched to room temperature with the quenching rate of 20 °C/s. The martensite start (M_s) temperature of 301 °C and martensite finish (M_f) temperature of 200 °C were determined experimentally for the studied steel in an earlier study [39].

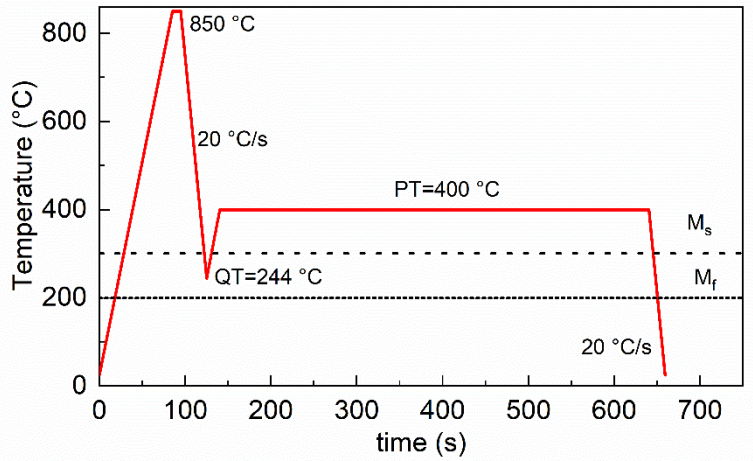

Fig. 1. Schematic illustration of Q&P heat treatment cycle applied to the studied steel.

2.2. Static and dynamic tensile tests

For both the static and dynamic tests, dog-bone shaped tensile specimens with a

gauge length of 6 mm, a width of 3 mm, a fillet radius of 1 mm and a thickness of 1 mm machined by spark erosion were used, as shown in Fig. 2a. The tensile axis is oriented along the rolling direction. A Zwick/Roell Z250 universal testing machine was employed to conduct the static tests at room temperature at constant strain rates of 1×10^{-4} and 1×10^{-2} s^{-1}.

To explore the mechanical behavior of materials at high strain rates, a split Hopkinson tensile bar (SHTB) was used. It is shown schematically in Fig. 2b [40]. The setup basically consists of two aluminum bars with a diameter of 25 mm, i.e. the input bar and output bar with lengths of 6 m and 3.125 m, respectively, between which the sample is fixed. Before a test, the impactor is accelerated towards the anvil at the free end of the input bar, thus generating an incident tensile wave in the input bar. The incident wave propagates along the input bar towards the sample and gives rise to a high strain rate deformation of the sample. By adjusting the impactor speed, the strain rate in the sample can be varied in the range of 100–5000 s^{-1}. In the present work, strain rates from ~500 s^{-1} to ~1000 s^{-1} are imposed. At least two specimens were tested for each condition, and the results were found to be reproducible. It should be noted that the Split Hopkinson tensile bar test technique, including the specimen geometry, is not standardized. Therefore, the geometry and dimensions were chosen based on considerations formulated in [40].

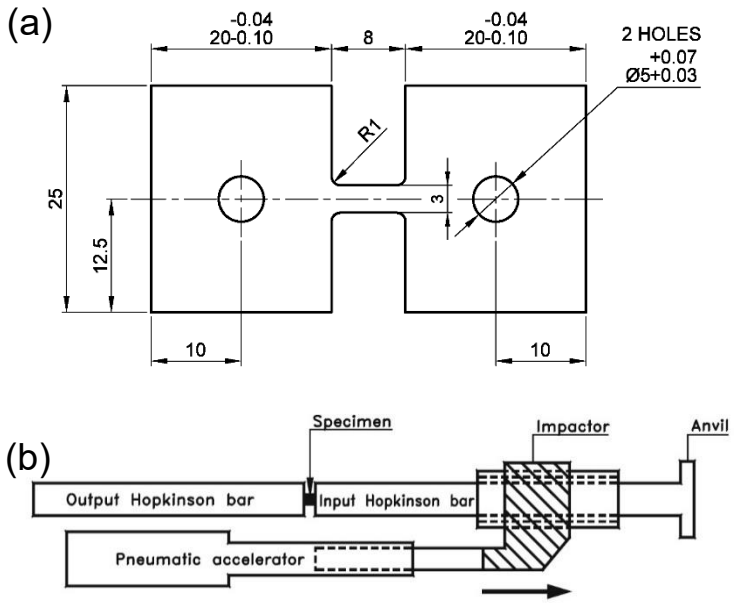

Fig. 2. (a) The geometry of specimens for static and dynamic tensile test; (b) Schematic presentation of the SHTB system.

The evolution of local strain during static and dynamic tensile tests was characterized using digital image correlation (DIC) technique. Prior to testing, black speckles were applied on the white painted specimen surface to generate a random black-white pattern. During testing, the deforming speckle pattern was recorded by two high speed cameras (FASTCAM Mini AX200, Photron) operating at 30000 frames per second. The spatial resolution of the recorded images was 256*624 pixels. From the images the strain fields on the sample surface were calculated using the commercial DIC software Vic-2D (Correlated Solutions Inc.). The subset and stepsize are 9 pixels and 1 pixel, respectively. An algorithm named normalized sum of squared differences (NSSD) was selected to obtain the strain value.

2.3. Microstructure and fractographic analysis

Electron backscatter diffraction (EBSD) technique was employed to characterize the evolution of microstructure during both static and dynamic tensile tests. A FEI Helios NanoLab 600i field emission gun scanning electron microscope (FEG-SEM), equipped with a NordlysNano detector controlled by the Aztec Oxford Instruments Nanoanalysis software (version 4.2®), was used for EBSD measurement. The FEG-SEM operating conditions were an accelerate voltage of 18 kV and a current intensity of 2.7 nA with a step size of 50 nm. HKL Channel 5 software (version 5.1®) was employed for post-processing and analyzing the orientation data. The positions of scanned areas are schematically shown in Fig. 3. The true strain ε in the EBSD measured position was calculated using the following equation:

$$\varepsilon = \ln \frac{A_0}{A_f} \quad (1)$$

where A_o is the original cross section of the gauge part and A_f the cross section after plastic deformation.

Specimens were thinned to the half of thickness to avoid the influence of local strain non-uniformity. After that, the standard metallographic procedures and final

polishing with OP-U for 10 minutes were applied to obtain a flat surface and to remove the possible surface deformed layer.

Cross-sectional TEM lamellar for specimen after SHTB testing were prepared via focused ion beam (FIB) technique in a FIB-FEGSEM dual-beam microscope (Helios NanoLab 600i, FEI). The TEM sample was taken from the area close to fracture. TEM characterization was carried out in a FEG S/TEM microscope (Talos F200X, FEI) operating at 200 KV

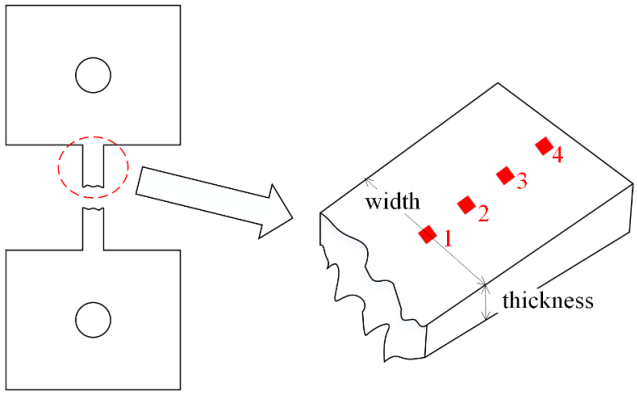

Fig. 3. Schematic presentation of the areas (marked by red squares) scanned by EBSD and the measurement of width and thickness after SHTB testing. The spacing between different areas was about 900 μm, and the first area was about 1 mm away from the fracture surface.

3. Results and discussion

3.1. Mechanical properties

Two representative engineering strain-stress curves of the studied Q&P steel during static and SHTB tests at strain rates of 10^{-2} s^{-1} and 727 s^{-1}, respectively, are shown in Fig. 4a. In both static and dynamic conditions, no clear yield plateau is observed. Plastic hardening is limited in both conditions. After reaching the maximum flow stress, onset of necking occurs followed by specimen failure.

Elongation to failure as a function of strain rate is presented in Fig. 4b. For all tensile tests in static or dynamic conditions, the maximum total elongation values are essentially in the same range (0.24 – 0.28), though the results from dynamic tests (750 s^{-1} and 1000 s^{-1}) show a higher scatter. Two explanations for the latter observation are

proposed. First, it can be related to the features of testing using high speed SHTB system. Oscillation always has some influence on the results in high strain rate tensile experiments, deriving from the extremely short interacting time (0.3 – 0.6 ms in this study) between the stress wave and the specimens [41]. Second, it might be related to the combined result of suppression of DARA (dislocation absorption of retained austenite) effect and the softening effect of adiabatic heating, as reported in [42]. The DARA refers to the fact that dislocations in martensite can be absorbed by retained austenite, making the martensite softer and intensifying its formability. However, the DARA effect is suppressed during dynamic loading because of lack of time for dislocation migration from martensite into austenite, which is unfavorable for the deformation ability. As a result, the total elongation will decrease when the adiabatic softening cannot compensate the absence of DARA [42].

The variations of yield strength (YS) and ultimate tensile strength (UTS) with strain rate during static and dynamic tensile tests are plotted in Fig. 4c and d, respectively. The YS of the Q&P treated steel shows similar values at static conditions and increases by more than 200 MPa for the case of dynamic tests (500 s^{-1}–1000 s^{-1}). The UTS of the studied steel shows a moderate linear increase from the lowest strain rate (10^{-2} s^{-1}) to the highest strain rate (10^{3} s^{-1}). The increasing strength of the Q&P steel during high strain rate deformation can be ascribed to two aspects: (1) strain rate hardening effect from dislocation gliding and (2) acceleration of TRIP effect from RA transformation. According to the widely used Johnson-Cook model [43], the deformation resistance increases linearly with the logarithm of strain rate due to insufficient dislocation glide. On the other hand, Zou et al. [44] reported that austenite-martensite transformation during high strain rate deformation was accelerated by the increased number of dislocations and shear band intersections significantly promoting phase transformation. Our results clearly demonstrate that the RA fraction decreases exponentially with strain showing the TRIP acceleration effect (see section 3.3). Therefore, the combined effect of dislocations and TRIP leads to enhanced strength of the studied Q&P steel at high strain rates.

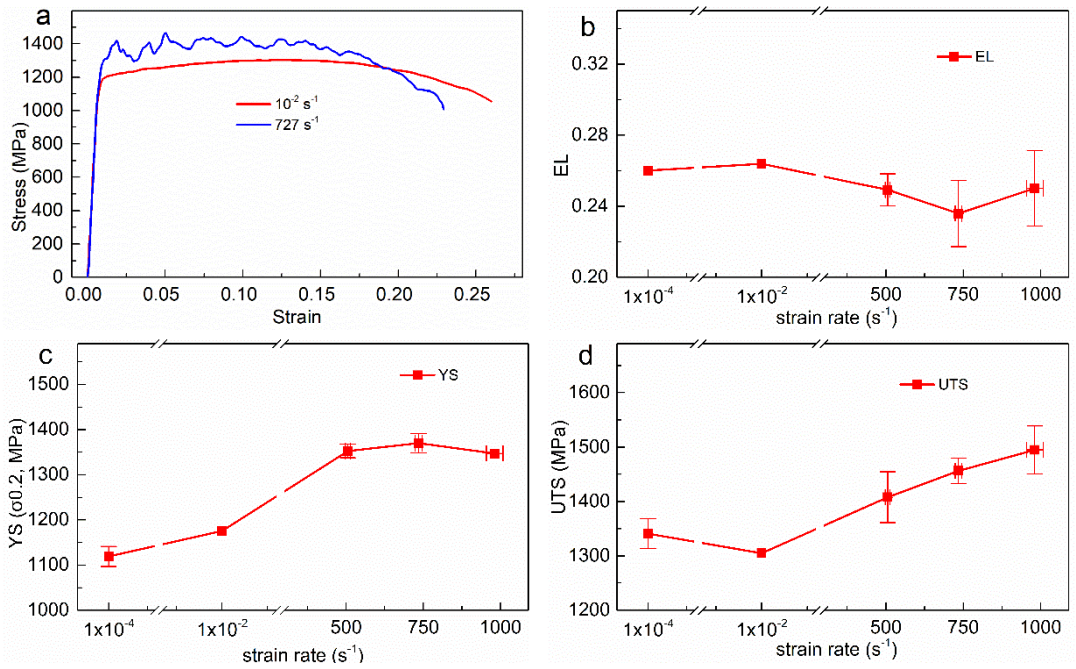

Fig. 4. (a) Typical engineering stress-strain curves from static and SHTB tests. (b), (c) and (d) are the elongation (EL), yield strength (YS) and ultimate tensile strength (UTS) versus different strain rates for the studied Q&P steel.

3.2. Local plastic strain

Figure 5 represents a selection of typical images taken by high speed camera during a test of a specimen with high strain rate of 511 s^{-1} from undeformed condition (at 0 μs) to final failure stage (at 433 μs). Corresponding maps of strain distribution are overlaid. It is clearly seen that before 300 μs, the axial strain field in the central gauge section of the specimen is homogeneous without any evidence of strain localization before a strain of about ~17.5 % (Fig. 5c). Areas of localized strain appear on the central part of the maps with increasing time (from 300 μs) which indicates onset of necking. Further deformation is localized within the necking area (Fig. 5d–f). The highest value of the local strain is 68% (Fig. 5f), while the strain averaged over the gauge section at fracture obtained from the SHTB signals varies between 24%–28% (Fig. 4b). Next to the neck, the latter values includes the strain of areas out of neck [45,46]. The corresponding stress-strain curve is also presented Fig. 5g, where arrows indicate the time when the photos (Fig. 5a–f) were captured.

To analyze the strain distribution along the tensile axis during high strain rate

deformation, the strain data was extracted from DIC and averaged for each cross section perpendicular to the tensile direction. The outcome of this analysis is shown in Fig. 6. A homogeneous strain distribution along the tensile axis over the gage length is observed until 267 μs, when reaching a strain value in the center of ~0.17 which is relevant to the maps of plastic strain distribution presented in Fig. 5. The peaks on the curve for 300 μs (with strain about 0.22) indicate the onset of strain localization and necking, which becomes more pronounced upon further loading. Comparison of the local plastic strain evolution during dynamic and static tensile deformation did not show any significant differences in deformation behavior on the meso-scale. It is also similar to that observed during tensile deformation of TWIP steel in [45].

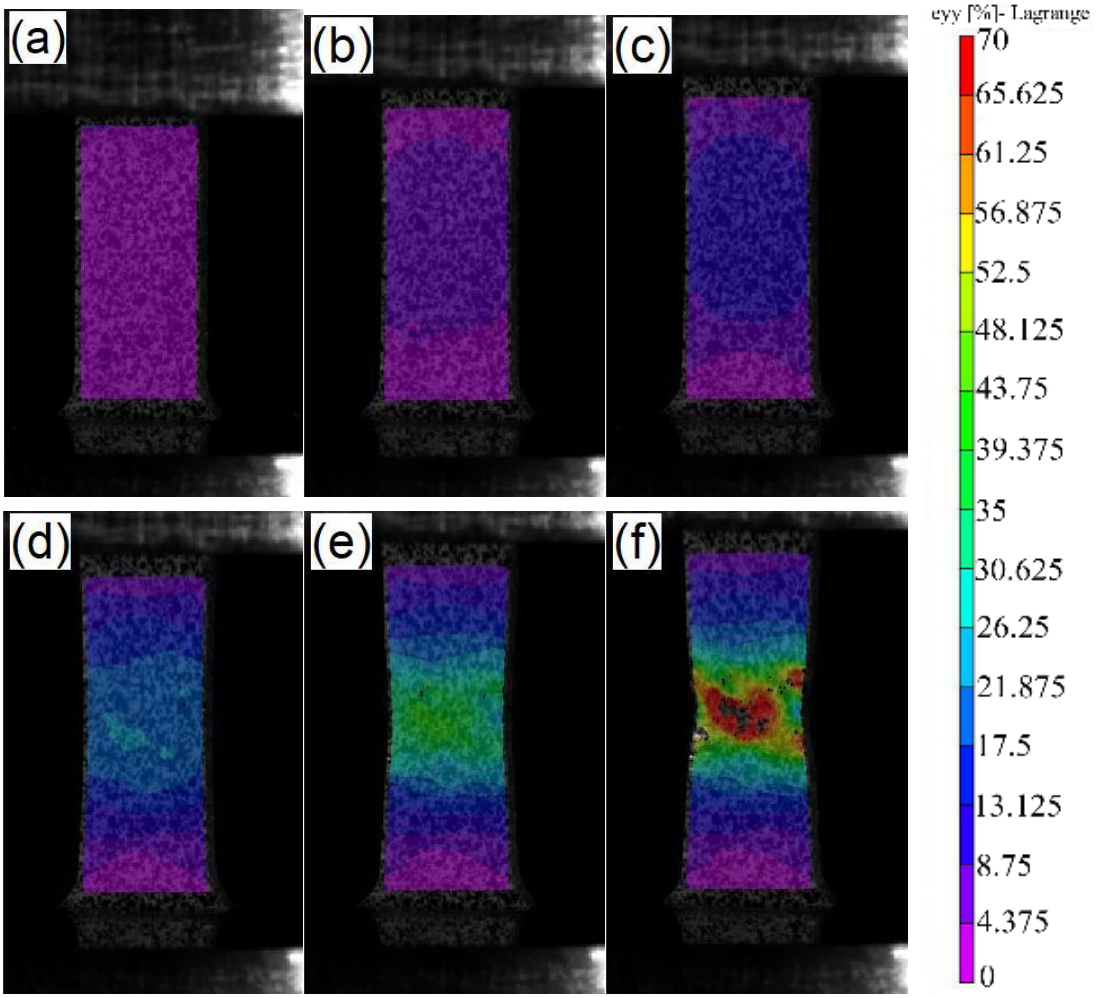

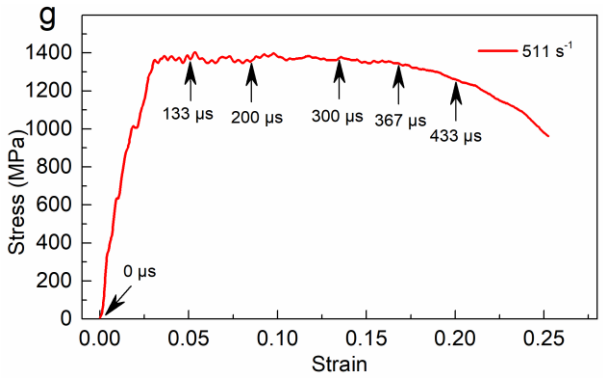

Fig. 5. Axial strain distribution obtained by DIC during a SHTB test at different times: (a) 0 μs, (b) 133 μs, (c) 200 μs, (d) 300 μs, (e) 367 μs, (f) 433 μs. (g) The corresponding strain-stress curve for Fig.5a to f. Arrows indicate times. The sample was tested at strain rate of 511 s^{-1}. (For interpretation of the references to color in this figure legend, the reader is referred to the Web version of this article.)

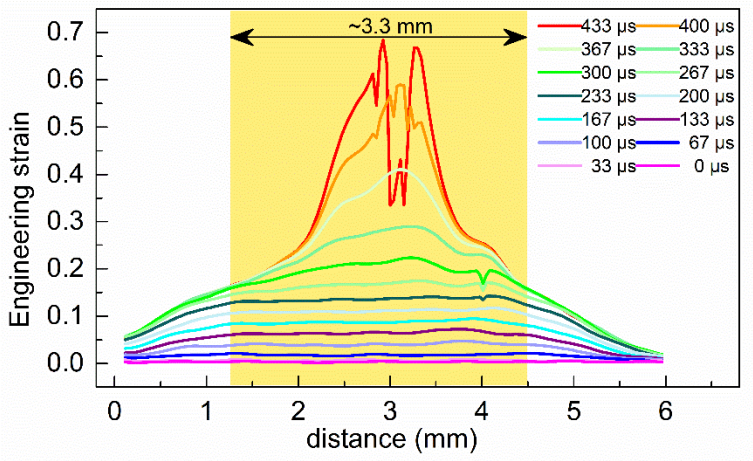

Fig. 6. Typical distribution of axial strain calculated by DIC technique along the tensile axis in a SHTB test. The sample was tested at a strain rate of 511 s^{-1}. The horizontal axis represents the position along the tensile direction. The strain is an average value for all data of the considered cross section. (For interpretation of the references to color in this figure legend, the reader is referred to the Web version of this article.)

3.3. Microstructure evolution

Band contrast maps in grey scale superimposed with fcc (austenite) phase map in green color for the studied steel before and after SHTB testing are shown in Fig. 7. In the undeformed sample (Fig. 7a), tempered martensite (TM) and untempered martensite (UM, marked by red arrows in Fig. 7a) can be distinguished due to their difference in

grey scale, where TM is brighter than UM. This results from significant difference in lattice defect density between these two kinds of martensite, and the Kikuchi pattern quality is significantly dependent on the lattice distortion. Because of partitioning process (for 500 s at 400 °C), TM has a lower dislocation density than UM. Two morphologies of RA are observed on the EBSD maps of the undeformed specimen: large blocky RA grains having a size of ~1–2 μm and finer lamellar-type ones. The finest RA laths formed between martensite grains have a thickness of 20–100 nm, and part of them cannot be observed via EBSD [47,48], as the step size of EBSD technique used in this study is 50 nm. Very thin interlath RA having a thickness of 10–20 nm, which cannot be detected by EBSD, is also present in the material [24]. We observed such interlath RA in TEM images as shown in Fig 8. Dark field images clearly reveal the existence of very thin interlath RA grains (marked by red circle on Fig. 8b) between martensite laths (marked by red circle on Fig. 8c). Prior austenite grain boundaries can also be clearly seen in the microstructure of the undeformed sample, and most RA grains are located in these high angle boundaries (>15 °). Earlier studies of Q&P steels using transmission electron microscopy have confirmed that both TM and UM are dislocation type martensite [49]. And the TEM characterization also shows that the TM has a lath thickness about 0.2–0.3 μm while UM has a smaller thickness, around 0.1–0.2 μm [24], as TM is formed from the first quenching and has larger parent grain size. It has also been figured out by selected area electron diffraction (SAED) that martensite laths in Q&P steel has K-S relationship ($(\bar{1}\,\bar{1}\,0)_\alpha//(\bar{1}\,1\,\bar{1})_\gamma$, $[001]_\alpha//[011]_\gamma$) with the parent austenite as presented in the former literature [42]. It should be noted that the microstructure was found to be homogeneous through the thickness of the Q&P treated sheet.

Volume fraction of RA dramatically decreases with increasing plastic strain during high strain rate deformation (Fig. 7). The coarse RA blocks transform into martensite first, and only ultrafine RA grains remain in the microstructure, as shown in Fig. 7(b) to (d). Quantitative analysis of RA volume fraction after high strain rate tensile testing shows that it decreases exponentially with plastic strain, which means that most RA

grains transform into martensite at the early stage of plastic deformation, which is referred to as acceleration of TRIP effect (Section 3.1). A representative plot of RA volume fraction vs. true plastic strain is presented in Fig. 9. It is clearly seen that the RA volume fraction decreased from 9.5% to 2.2% with increasing true strain from 0% (undeformed) to 16%. Nonlinear fitting of the experimental results shows exponential character of their relationship with the R-Square of 0.984. A constant of 1.66 obtained from the fitting equation indicates that at least 1.66% of RA would remain untransformed regardless of the plastic strain which can be related to the very fine interlath RA having very high stability during plastic deformation [47]. Similar results were also reported by Yang et al. [28] in the study of the relationship between RA volume fraction and plastic strain during dynamic deformation of a Q&P 980 steel and for the given Q&P steel subjected to drop weight impact testing [50]. TEM examination in the present study also revealed interlath austenite in the necking area close to the fracture surface after high strain rate deformation, as shown in Fig. 8b, demonstrating its high stability. By employing a modified SHTB system, which allows to induce the predetermined plastic strain during high strain rate testing, they could precisely measure the effect of plastic strain on the RA volume fraction via synchrotron XRD. Their results showed that after deformation to plastic strain of 15% at strain rate of 1000 s^{-1}, the RA fraction decreased from 12% to 4%, which is close to the values reported in the present study.

There are more publications on the effect of plastic strain on RA volume fraction in AHSSs during their static tensile deformation, several investigations have already been conducted. Hao et al. [42] measured the evolution of RA volume fraction in a quenched-partitioned-tempered steel after deformation to various plastic strain values using XRD technique. The RA volume fraction decreased exponentially from 10.8% to 3.0% with increasing plastic strain from zero to 11%. In another investigation on Q&P treated steel (with the same chemical composition as in the present study) by Knijf et al. [51], as shown in Fig. 9, the RA volume fraction also decreased exponentially with increasing plastic strain. Therefore, it can be outlined that the RA volume fraction in the Q&P steels has the similar dependence on the plastic strain during both static and

dynamic tensile testing, and its fraction exponentially decreases with increasing plastic strain.

The fraction of UM in the microstructure increases with increasing plastic strain. However, it is hard to distinguish between UM and TM grains in the band contrast maps of the deformed material (Fig. 7b,c,d). The UM grains have a higher hardness due to the higher carbon content. Therefore, plastic deformation is accumulated in softer tempered martensitic grains [52,53] increasing dislocation density and lattice distortion therein which, in turn, leads to low band contrast. Therefore, the difference in band contrast between fresh and tempered martensite is minimized, and it is much harder (or even impossible) to separate them using band contrast maps in the deformed material.

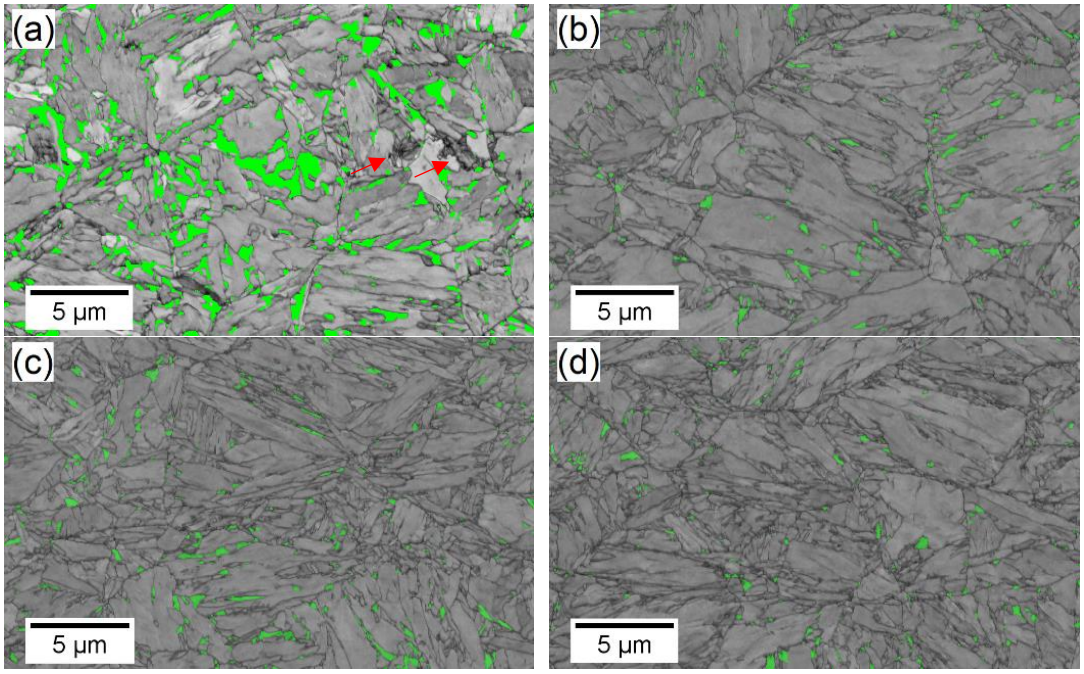

Fig. 7. Typical band contrast maps (combined with RA phase maps) for the studied Q&P steel at different true plastic strain: (a) 0, (b) 11.48%, (c) 16.66% and (d) 29.92%. The specimen was tested at strain rate of 511 s^{-1}. Red arrows in Fig. 7(a) refers to untempered martensite. (For interpretation of the references to color in this figure legend, the reader is referred to the Web version of this article.)

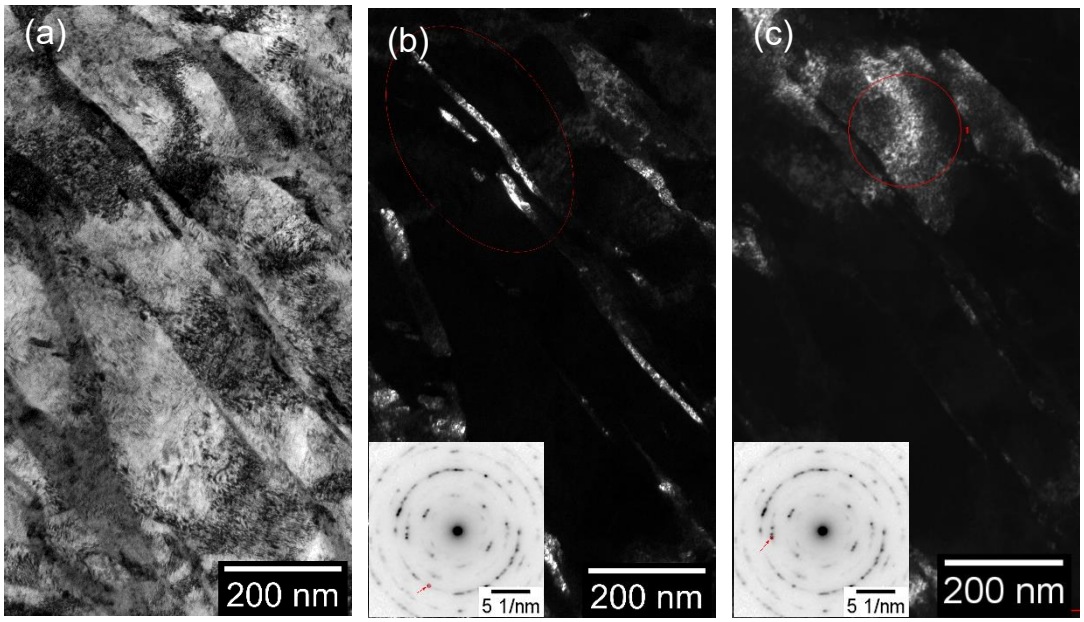

Fig. 8. TEM images taken from the necking area close to the fracture surface of the sample tested at a strain rate of 511 s^{-1}. (a) Bright field (BF) image, (b) dark field (DF) image interlath austenite, (c) DF image of martensite. Selected diffraction spots are marked with red color in the inserted diffraction patterns in (b) and (c), respectively.

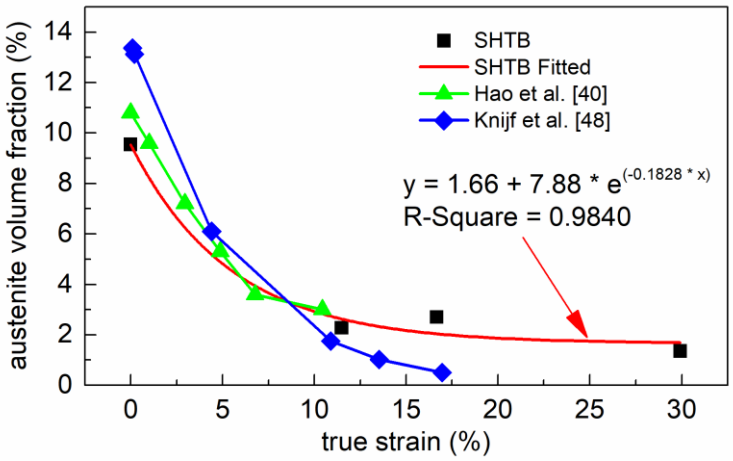

Fig. 9. Evolution of RA volume fraction with true plastic strain. Data from literature have also been plotted for comparison.

3.4. Fracture surface

In order to understand the failure behavior of the studied Q&P steel at different testing strain rates, the fracture surfaces were examined using scanning electron microscope (SEM). Fractographs of samples after static and dynamic tensile testing are shown in Fig. 10. It is seen that at all strain rates, the samples failed in ductile mode.

Indeed, all fracture surfaces show a similar morphology consisting of small, shallow and nonuniform dimples, which were developed through nucleation, growth, and coalescence of microvoids. The dimple size was statistically measured using the linear intercept counting method (ASTM E112), and 35–45 SEM images (4000x magnification) were used to guarantee the reliability of the results. The histograms of dimple size distribution for samples tested at different strain rates are plotted in Fig. 11. It is clearly seen that the fracture surfaces of samples after static tensile testing (1×10^{-4} and 1×10^{-2} s^{-1}) show somewhat coarser dimples compared to the samples after dynamic testing (500–1000 s^{-1}). During low strain rate deformation, microvoids have sufficient time for growth with respect to the short time (0.3–0.6 ms) during high strain rate deformation.

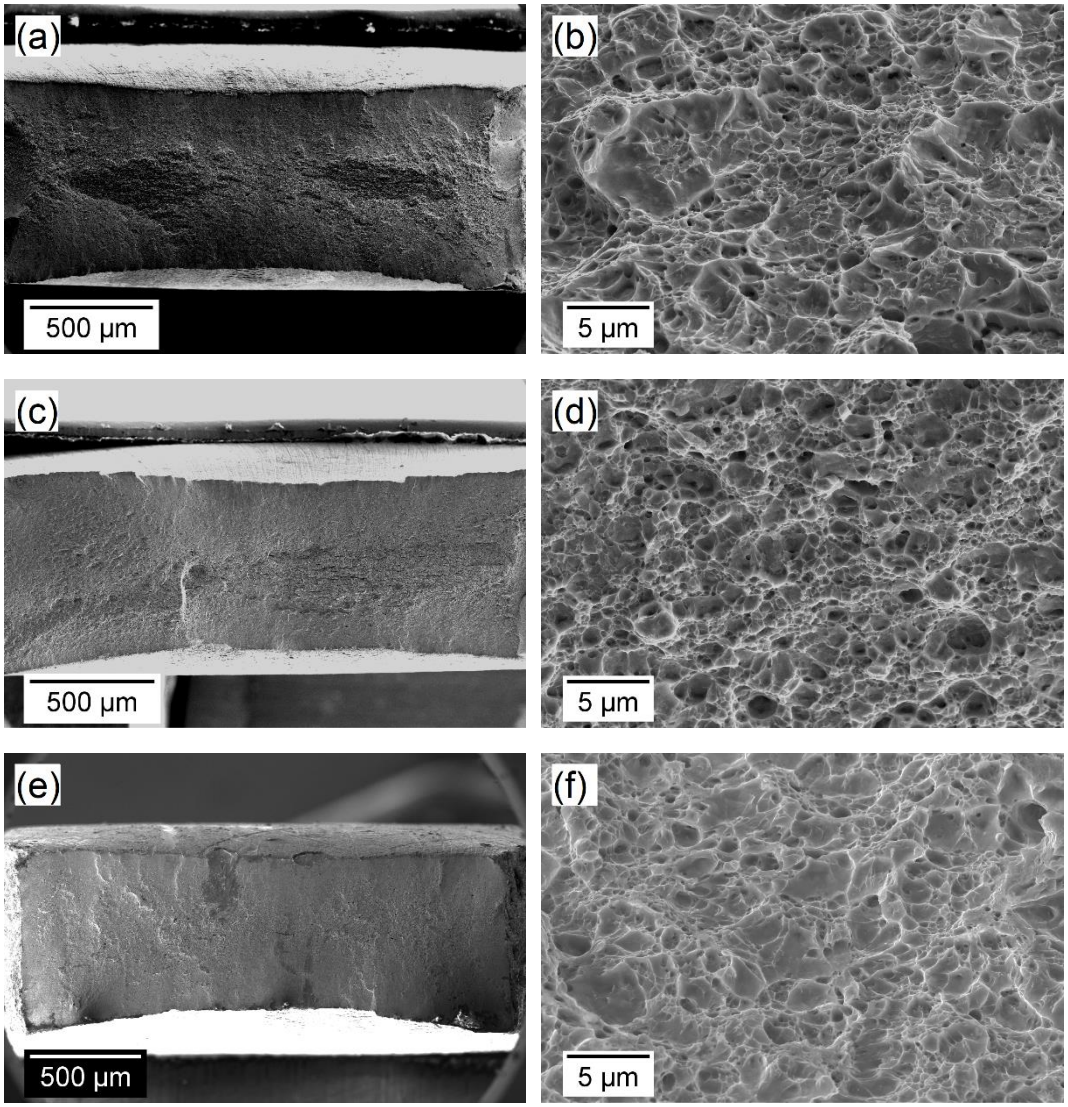

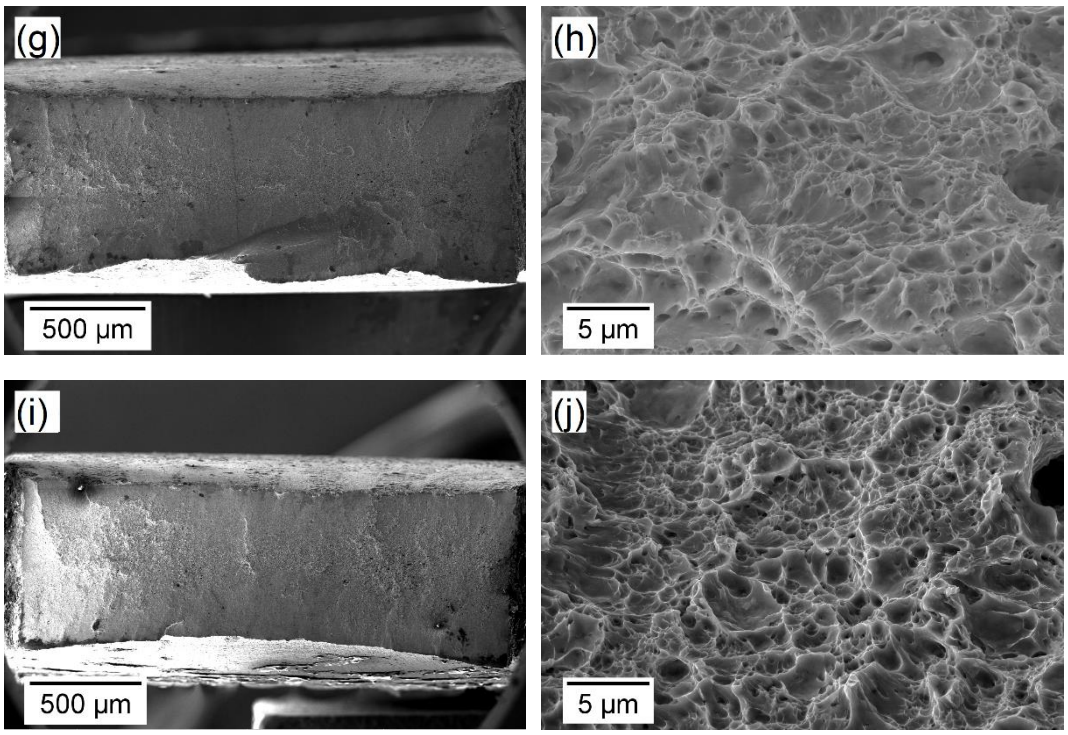

Fig. 10. Typical SEM images of fracture surface of the studied Q&P steel tested at strain rate of: (a, b) 1×10^{-4} s^{-1}, (c, d) 1×10^{-2} s^{-1}, (e, f) 511 s^{-1}, (g, h) 742 s^{-1} and (i, j) 962 s^{-1}.

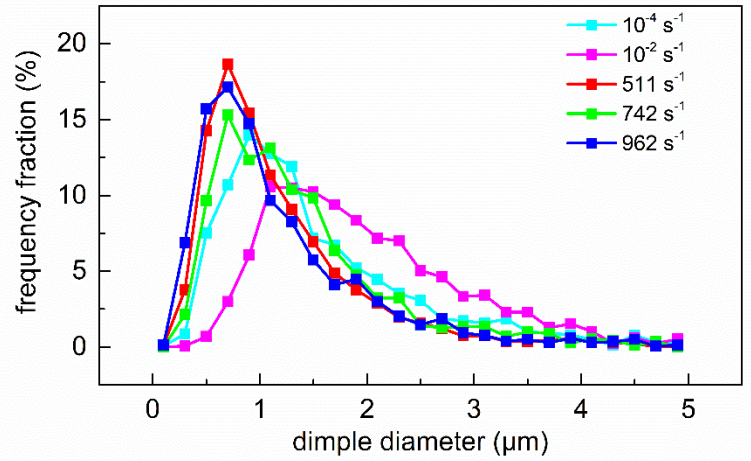

Fig. 11. Histograms of dimple size distribution on the fracture surface of the Q&P steel tested at different strain rates. (For interpretation of the references to color in this figure legend, the reader is referred to the Web version of this article.)

It should be noted that quasi-cleavage and brittle fracture were also reported for some Q&P processed steels [54]. The fracture surface of the Q&P steels is to great

extent determined by the tempered condition of the martensitic matrix. In our case, the martensitic matrix was tempered at relatively high temperature (400 ^{o}C) for relatively long time (500 s), resulting in its fracture by ductile mode. In our earlier work [55], we have thoroughly studied the fracture behavior of this Q&P treated steel. Quantitative 3D analysis of the fracture surface of the double-edge notched tensile specimens using state-of-the-art characterization techniques clearly revealed ductile fracture mode. In the meanwhile, significant fraction of fracture surface of this steel tempered at lower temperature 280 ^{o}C for less than 1 s (resulting in less tempered martensitic matrix) showed quasi-cleavage character [55].

4. Conclusions

The high strain rate deformation behavior of a Q&P processed Fe-0.25C-1.5Si-3.0Mn (wt. %) steel containing martensitic matrix and retained austenite was investigated via SHTB testing system. Tensile tests at conventional strain rates were also carried out for comparison. Analysis of mechanical properties, microstructural evolution and failure behavior was performed. The following conclusions can be drawn based on the experimental results.

1. The Q&P treated steel shows higher yield strength (by > 200 MPa) during high strain rate tensile deformation. Its ultimate tensile strength increases linearly with strain rate. The total elongation shows an opposite trend. The strength increase at high strain rates is ascribed to enhanced strain rate hardening and acceleration of TRIP effect.

2. The maps of local strain distribution generated by DIC technique indicate that the specimens are deformed homogeneously over the gage section before the plastic strain of 0.16 during both dynamic and static tensile testing.

3. EBSD characterization of microstructure shows that the RA volume fraction decreases exponentially with plastic strain during high strain rate tensile deformation, similar to the case of static tensile testing.

4. SEM examination of the fracture surface of tested samples indicate failure in ductile mode. Shallow and nonuniform dimples are the main features of specimens

tested at all strain rates, and the dimple size is slightly higher in the specimens after static tensile testing due to longer time available for dimples to grow during static tensile testing.

Acknowledgements

This work was financially supported by the OptiQPAP project funded by RFCS within Horizon 2020 Program (Grant Agreement 709755). Peikang Xia acknowledges gratefully the financial supporting from Chinese Scholarship Council (No. 201606890031).

References

[1] Y. Tomita, T. Iwamoto, Constitutive modeling of trip steel and its application to the improvement of mechanical properties, Int. J. Mech. Sci. 37 (1995) 1295–1305. doi:10.1016/0020-7403(95)00039-Z.

[2] S. Zaefferer, J. Ohlert, W. Bleck, A study of microstructure, transformation mechanisms and correlation between microstructure and mechanical properties of a low alloyed TRIP steel, Acta Mater. 52 (2004) 2765–2778. doi:10.1016/j.actamat.2004.02.044.

[3] I. Gutierrez-Urrutia, S. Zaefferer, D. Raabe, The effect of grain size and grain orientation on deformation twinning in a Fe–22wt.% Mn–0.6wt.% C TWIP steel, Mater. Sci. Eng. A. 527 (2010) 3552–3560. doi:10.1016/j.msea.2010.02.041.

[4] S. Vercammen, B. Blanpain, B.C. De Cooman, P. Wollants, Cold rolling behaviour of an austenitic Fe–30Mn–3Al–3Si TWIP-steel: the importance of deformation twinning, Acta Mater. 52 (2004) 2005–2012. doi:10.1016/j.actamat.2003.12.040.

[5] S. Curtze, V.-T. Kuokkala, M. Hokka, P. Peura, Deformation behavior of TRIP and DP steels in tension at different temperatures over a wide range of strain rates, Mater. Sci. Eng. A. 507 (2009) 124–131. doi:10.1016/j.msea.2008.11.050.

[6] J. Hu, L.-X. Du, J.-J. Wang, C.-R. Gao, T.-Z. Yang, A.-Y. Wang, R.D.K. Misra, Microstructures and Mechanical Properties of a New As-Hot-Rolled High-Strength DP Steel Subjected to Different Cooling Schedules, Metall. Mater. Trans. A. 44 (2013) 4937–4947. doi:10.1007/s11661-013-1839-z.

[7] A.J. Clarke, J.G. Speer, D.K. Matlock, F.C. Rizzo, D.V. Edmonds, M.J. Santofimia, Influence of carbon partitioning kinetics on final austenite fraction during quenching and partitioning, Scr. Mater. 61 (2009) 149–152. doi:10.1016/j.scriptamat.2009.03.021.

[8] M.J. Santofimia, L. Zhao, R. Petrov, C. Kwakernaak, W.G. Sloof, J. Sietsma, Microstructural development during the quenching and partitioning process in a newly designed low-carbon steel, Acta Mater. 59 (2011) 6059–6068. doi:10.1016/j.actamat.2011.06.014.

[9] J. Speer, D.K. Matlock, B.C. De Cooman, J.G. Schroth, Carbon partitioning into austenite after martensite transformation, Acta Mater. 51 (2003) 2611–2622. doi:10.1016/S1359-

6454(03)00059-4.

[10] H.Y. Li, X.W. Lu, X.C. Wu, Y.A. Min, X.J. Jin, Bainitic transformation during the two-step quenching and partitioning process in a medium carbon steel containing silicon, Mater. Sci. Eng. A. 527 (2010) 6255–6259. doi:10.1016/j.msea.2010.06.045.

[11] J.G. Speer, D.V. Edmonds, F.C. Rizzo, D.K. Matlock, Partitioning of carbon from supersaturated plates of ferrite, with application to steel processing and fundamentals of the bainite transformation, Curr. Opin. Solid State Mater. Sci. 8 (2004) 219–237. doi:10.1016/j.cossms.2004.09.003.

[12] D. De Knijf, R. Petrov, C. Föjer, L.A.I. Kestens, Effect of fresh martensite on the stability of retained austenite in quenching and partitioning steel, Mater. Sci. Eng. A. 615 (2014) 107–115. doi:10.1016/j.msea.2014.07.054.

[13] X.D. Wang, Z.H. Guo, Y.H. Rong, Mechanism exploration of an ultrahigh strength steel by quenching–partitioning–tempering process, Mater. Sci. Eng. A. 529 (2011) 35–40. doi:10.1016/j.msea.2011.08.050.

[14] L. Wang, J.G. Speer, Quenching and Partitioning Steel Heat Treatment, Metallogr. Microstruct. Anal. 2 (2013) 268–281. doi:10.1007/s13632-013-0082-8.

[15] W. Wang, M. Li, C. He, X. Wei, D. Wang, H. Du, Experimental study on high strain rate behavior of high strength 600–1000MPa dual phase steels and 1200MPa fully martensitic steels, Mater. Des. 47 (2013) 510–521. doi:10.1016/j.matdes.2012.12.068.

[16] E. Cadoni, M. Dotta, D. Forni, P. Spätig, Strain-rate behavior in tension of the tempered martensitic reduced activation steel Eurofer97, J. Nucl. Mater. 414 (2011) 360–366. doi:10.1016/j.jnucmat.2011.05.002.

[17] A.K. Roy, S.R. Kukatla, B. Yarlagadda, V.N. Potluri, M. Lewis, M. Jones, B.J. O'Toole, Tensile properties of martensitic stainless steels at elevated temperatures, J. Mater. Eng. Perform. 14 (2005) 212–218. doi:10.1361/10599490523373.

[18] I.D. Choi, D.M. Bruce, S.J. Kim, C.G. Lee, S.H. Park, D.K. Matlock, J.G. Speer, Deformation Behavior of Low Carbon TRIP Sheet Steels at High Strain Rates, ISIJ Int. 42 (2002) 1483–1489. doi:10.2355/isijinternational.42.1483.

[19] J.V. Slycken, P. Verleysen, J. Degrieck, L. Samek, B.C. de Cooman, High-strain-rate behavior of low-alloy multiphase aluminum- and silicon-based transformation-induced plasticity steels, Metall. Mater. Trans. A. 37 (2006) 1527–1539. doi:10.1007/s11661-006-0097-8.

[20] P. Sahu, S. Curtze, A. Das, B. Mahato, V.-T. Kuokkala, S.G. Chowdhury, Stability of austenite and quasi-adiabatic heating during high-strain-rate deformation of twinning-induced plasticity steels, Scr. Mater. 62 (2010) 5–8. doi:10.1016/j.scriptamat.2009.09.010.

[21] Z.Y. Liang, X. Wang, W. Huang, M.X. Huang, Strain rate sensitivity and evolution of dislocations and twins in a twinning-induced plasticity steel, Acta Mater. 88 (2015) 170–179. doi:10.1016/j.actamat.2015.01.013.

[22] M.J. Santofimia, L. Zhao, R. Petrov, J. Sietsma, Characterization of the microstructure obtained by the quenching and partitioning process in a low-carbon steel, Mater. Charact. 59 (2008) 1758–1764. doi:10.1016/j.matchar.2008.04.004.

[23] J.G. Speer, E.D. Moor, K.O. Findley, D.K. Matlock, B.C.D. Cooman, D.V. Edmonds, Analysis of Microstructure Evolution in Quenching and Partitioning Automotive Sheet Steel, Metall. Mater. Trans. A. 42 (2011) 3591. doi:10.1007/s11661-011-0869-7.

[24] C.Y. Wang, J. Shi, W.Q. Cao, H. Dong, Characterization of microstructure obtained by

quenching and partitioning process in low alloy martensitic steel, Mater. Sci. Eng. A. 527 (2010) 3442–3449. doi:10.1016/j.msea.2010.02.020.

[25] E. Paravicini Bagliani, M.J. Santofimia, L. Zhao, J. Sietsma, E. Anelli, Microstructure, tensile and toughness properties after quenching and partitioning treatments of a medium-carbon steel, Mater. Sci. Eng. A. 559 (2013) 486–495. doi:10.1016/j.msea.2012.08.130.

[26] H. Liu, X. Lu, X. Jin, H. Dong, J. Shi, Enhanced mechanical properties of a hot stamped advanced high-strength steel treated by quenching and partitioning process, Scr. Mater. 64 (2011) 749–752. doi:10.1016/j.scriptamat.2010.12.037.

[27] C. Liu, L. Wang, Y. Liu, Effects of Strain Rate on Tensile Deformation Behavior of Quenching and Partitioning Steel, Mater. Sci. Forum. 749 (2013) 401–406. doi:10.4028/www.scientific.net/MSF.749.401.

[28] X. Yang, X. Xiong, Z. Yin, H. Wang, J. Wang, D. Chen, Interrupted Test of Advanced High Strength Steel with Tensile Split Hopkinson Bar Method, Exp. Mech. 54 (2014) 641–652. doi:10.1007/s11340-013-9828-0.

[29] E.D. Moor, J.G. Speer, D.K. Matlock, J.-H. Kwak, S.-B. Lee, Effect of Carbon and Manganese on the Quenching and Partitioning Response of CMnSi Steels, ISIJ Int. 51 (2011) 137–144. doi:10.2355/isijinternational.51.137.

[30] M. Calcagnotto, D. Ponge, D. Raabe, On the Effect of Manganese on Grain Size Stability and Hardenability in Ultrafine-Grained Ferrite/Martensite Dual-Phase Steels, Metall. Mater. Trans. A. 43 (2012) 37–46. doi:10.1007/s11661-011-0828-3.

[31] J. Hidalgo, K.O. Findley, M.J. Santofimia, Thermal and mechanical stability of retained austenite surrounded by martensite with different degrees of tempering, Mater. Sci. Eng. A. 690 (2017) 337–347. doi:10.1016/j.msea.2017.03.017.

[32] A. Pichler, S. Traint, T. Hebesberger, P. Stiaszny, E.A. Werner, Processing of thin sheet multiphase steel grades, Steel Res. Int. 78 (2007) 216–223. doi:10.1002/srin.200705883.

[33] A. Grajcar, M. Kamińska, M. Opiela, P. Skrzypczyk, B. Grzegorczyk, E. Kalinowska-Ozgowicz, Segregation of alloying elements in thermomechanically rolled medium-Mn multiphase steels, J. Achiev. Mater. Manuf. Eng. 55 (2012) 256–264.

[34]H.K.D.H. Bhadeshia, D.V. Edmonds, The bainite transformation in a silicon steel, Metall. Trans. A. 10 (1979) 895–907. doi:10.1007/BF02658309.

[35] J. Tobata, K.-L. Ngo-Huynh, N. Nakada, T. Tsuchiyama, S. Takaki, Role of Silicon in Quenching and Partitioning Treatment of Low-carbon Martensitic Stainless Steel, ISIJ Int. 52 (2012) 1377–1382. doi:10.2355/isijinternational.52.1377.

[36] J. Maki, J. Mahieu, B.C.D. Cooman, S. Claessens, Galvanisability of silicon free CMnAl TRIP steels, Mater. Sci. Technol. 19 (2003) 125–131. doi:10.1179/026708303225009300.

[37] S. Traint, A. Pichler, K. Hauzenberger, P. Stiaszny, E. Werner, Influence of silicon, aluminium, phosphorus and copper on the phase transformations of low alloyed TRIP-steels, Steel Res. 73 (2002) 259–266. doi:10.1002/srin.200200206.

[38] S.-J. Kim, C. Gil Lee, T.-H. Lee, C.-S. Oh, Effect of Cu, Cr and Ni on mechanical properties of 0.15 wt.% C TRIP-aided cold rolled steels, Scr. Mater. 48 (2003) 539–544. doi:10.1016/S1359-6462(02)00477-3.

[39] D.D. Knijf, E.P.D. Silva, C. Föjer, R. Petrov, Study of heat treatment parameters and kinetics of quenching and partitioning cycles, Mater. Sci. Technol. 31 (2015) 817–828. doi:10.1179/1743284714Y.0000000710.

[40] P. Verleysen, J. Degrieck, T. Verstraete, J.V. Slycken, Influence of Specimen Geometry on Split Hopkinson Tensile Bar Tests on Sheet Materials, Exp. Mech. 48 (2008) 587. doi:10.1007/s11340-008-9149-x.

[41] P.S. Follansbee, C. Frantz, Wave Propagation in the Split Hopkinson Pressure Bar, J. Eng. Mater. Technol. 105 (1983) 61–66. doi:10.1115/1.3225620.

[42] Q. Hao, S. Qin, Y. Liu, X. Zuo, N. Chen, W. Huang, Y. Rong, Effect of retained austenite on the dynamic tensile behavior of a novel quenching-partitioning-tempering martensitic steel, Mater. Sci. Eng. A. 662 (2016) 16–25. doi:10.1016/j.msea.2016.03.007.

[43] G.R. Johnson, W.H. Cook, A constitutive model and data for metals subjected to large strains, high strain rates and high temperatures, in: Proc. 7th Int. Symp. Ballist., The Hague, The Netherlands, 1983: pp. 541–547.

[44] D.Q. Zou, S.H. Li, J. He, Temperature and strain rate dependent deformation induced martensitic transformation and flow behavior of quenching and partitioning steels, Mater. Sci. Eng. A. 680 (2017) 54–63. doi:10.1016/j.msea.2016.10.083.

[45] M. Kang, J. Park, S.S. Sohn, H.S. Kim, N.J. Kim, S. Lee, Interpretation of quasi-static and dynamic tensile behavior by digital image correlation technique in TWinning Induced Plasticity (TWIP) and low-carbon steel sheets, Mater. Sci. Eng. A. 693 (2017) 170–177. doi:10.1016/j.msea.2017.03.076.

[46] J. Qin, R. Chen, X. Wen, Y. Lin, M. Liang, F. Lu, Mechanical behaviour of dual-phase high-strength steel under high strain rate tensile loading, Mater. Sci. Eng. A. 586 (2013) 62–70. doi:10.1016/j.msea.2013.07.091.

[47] X.C. Xiong, B. Chen, M.X. Huang, J.F. Wang, L. Wang, The effect of morphology on the stability of retained austenite in a quenched and partitioned steel, Scr. Mater. 68 (2013) 321–324. doi:10.1016/j.scriptamat.2012.11.003.

[48] I.D. Diego-Calderón, D.D. Knijf, J.M. Molina-Aldareguia, I. Sabirov, C. Föjer, R. Petrov, Effect of Q&P parameters on microstructure development and mechanical behaviour of Q&P steels, Rev. Metal. 51 (2015) 035.

[49] F. Huang, J. Yang, Z. Guo, Y. Rong, N. Chen, Dynamic compression property of a low-carbon quenching and partitioning steel, Mater. Sci. Eng. A. 651 (2016) 224–232. doi:10.1016/j.msea.2015.10.115.

[50] P. Xia, I. Sabirov, J. Molina-Aldareguia, P. Verleysen, R. Petrov, Mechanical behavior and microstructure evolution of a quenched and partitioned steel during drop weight impact and punch testing, Mater. Sci. Eng. A. 737 (2018) 18–26. doi:10.1016/j.msea.2018.09.015.

[51] D. De Knijf, C. Föjer, L.A.I. Kestens, R. Petrov, Factors influencing the austenite stability during tensile testing of Quenching and Partitioning steel determined via in-situ Electron Backscatter Diffraction, Mater. Sci. Eng. A. 638 (2015) 219–227. doi:10.1016/j.msea.2015.04.075.

[52] I. de Diego-Calderón, M.J. Santofimia, J.M. Molina-Aldareguia, M.A. Monclús, I. Sabirov, Deformation behavior of a high strength multiphase steel at macro- and micro-scales, Mater. Sci. Eng. A. 611 (2014) 201–211. doi:10.1016/j.msea.2014.05.068.

[53] I. de Diego-Calderón, D. De Knijf, M.A. Monclús, J.M. Molina-Aldareguia, I. Sabirov, C. Föjer, R.H. Petrov, Global and local deformation behavior and mechanical properties of individual phases in a quenched and partitioned steel, Mater. Sci. Eng. A. 630 (2015) 27–35. doi:10.1016/j.msea.2015.01.077.

[54] F. Forouzan, M.A. Guitar, E. Vuorinen, F. Mücklich, Effect of Carbon Partitioning, Carbide Precipitation, and Grain Size on Brittle Fracture of Ultra-High-Strength, Low-Carbon Steel after Welding by a Quenching and Partitioning Process, Metals. 8 (2018) 747. doi:10.3390/met8100747.

[55] I. de Diego-Calderón, I. Sabirov, J.M. Molina-Aldareguia, C. Föjer, R. Thiessen, R.H. Petrov, Microstructural design in quenched and partitioned (Q&P) steels to improve their fracture properties, Mater. Sci. Eng. A. 657 (2016) 136–146. doi:10.1016/j.msea.2016.01.011.